

# CARNA – A Compact Glass Proton Imager

C. J. Wilkinson, L. Ruane, W. Miller, A. Gunsch, A. Zieser, I. J. Tillman, Z. Thune, D. Wang, and U. Akgun

**Abstract**—Protons deposit the majority of their energy at the end of their lifetimes, characterized by a Bragg peak. This makes proton therapy a viable way to target cancerous tissue while minimizing damage to surrounding healthy tissue. However, in order to utilize this high precision treatment, greater accuracy in tumor imaging is needed. An approximate uncertainty of  $\pm 3\%$  exists in the current practice of proton therapy due to conversions between x-ray and proton stopping power. An imaging system utilizing protons has the potential to eliminate that inaccuracy. This study focuses on developing a proof of concept proton-imaging detector built with a high-density glass scintillator.

## I. INTRODUCTION

THE hadron therapy centers' remarkable precision in dose delivery to cancerous cells give them an advantage over x-rays [1-12]. Due to their unique capability to avoid the healthy tissue they are demanded increasingly by patients. The therapy planning process requires exact calculations for the beam energy with the range needed to cover the tumor. Currently, X-ray CT images are used for this purpose, but their precision is compromised due to image noise and distortions, the stoichiometric calculations for Hounsfield Units, as well as the deviation of body tissue from standard radiation units of measure, mean excitation energy and the energy dependence of stopping power ratio (SPR). All these reasons cause a well-accepted variability rate of about 3.5% in the current practice of proton therapy. That beam-range uncertainty may cause the Bragg peak to overshoot or undershoot the tumor and damage adjacent healthy tissue [13-23].

One possible solution to this problem is to use the existing proton beam for imaging before therapy. This potentially will eliminate the errors originating from conversions between x-ray and proton interactions with matter. This report summarizes the efforts to design a compact proton imaging device that can be attached to the gantry. High-density, scintillating glass was chosen to be the active medium for this proton calorimeter, named **CARNA** (**C**ompact **g**lAss **p**roton **i**mager), after the roman goddess who protects and keeps healthy the vital organs, especially the lungs, liver and heart.

A previous study successfully designed and built a pCT (proton CT) detector prototype, by utilizing trackers, and a

crystal calorimeter [24,25]. CARNA's unique detector geometry and use of a pencil beam eliminate the tracker system, which makes the detector compact. Also using glass as the active medium provides room for improvement on geometry, cost effectiveness, and possibly on resolution.

This report also summarizes the efforts to develop novel high-density scintillating glass for this application. Since CARNA will be attached to a gantry, during the proton therapy it can also be used for *in vivo* imaging by detecting the prompt gamma particles generated within the patient body.

## II. NOVEL HIGH-DENSITY SCINTILLATING GLASS

Glass is a suitable material for particle detector applications; it is easy to produce and cost effective, and it can be designed both for virtually any geometry, and for fixed physical/optical/electrical properties depending on the need. For CARNA, we decided to develop a novel high-density scintillating glass. Theoretically, it is possible to make glass with a density of up to  $9.4 \text{ g/cm}^3$  in binary lead-bismuth systems; however previous studies do not report any results with higher than  $7.9 \text{ g/cm}^3$  of a non-scintillating glass<sup>27</sup>. Coe College glass research group successfully produced a non-scintillating glass with  $8.8 \text{ g/cm}^3$  density (unpublished data). The scintillating glasses generally suffer from low transfer efficiency and thus show a low light yield due to the presence of electron traps (possible centers of nonradiative recombination), which cause an inefficient transfer of the thermalized electrons and holes towards the emission centers. Using heavy metal oxide glasses will lower the frequency of the localized phonon mode, resulting in a higher likelihood of better light production and transmission efficiency. Cerium-doped silicate glasses especially seem to provide the highest light yield, about 6 photons/keV, and they give a host dependent band emission in the visible and near UV regions<sup>28</sup>.

In the Coe College glass laboratories various high-density scintillating glasses have been developed, specifically for this proton imager design. Since the imager detector is desired to be compact, the material development phase of the research has focused on high-density, oxide glasses containing tungsten, gadolinium, and doped with europium, terbium, and cerium.

The scintillating materials lose their UV transparency as they absorb more radiation. Among the various glass samples we have made, cerium doped samples have the least light yield with UV excitation. In addition, the emitted peak wavelength (390 nm) is very close to the transmission cutoff (370 nm). Furthermore, our current pCT scan plans require single spills of only  $10^6$  protons per second, which eliminates the fast signal advantage of cerium-doped glasses ( $\sim 10$  ns).

Manuscript received November 17, 2017. This work was supported by the National Science Foundation by the grant numbers NSF-DMR 1407404, NSF-REU 1358968.

C. Wilkinson, A. Gunsch, I. Tillman, Z. Thune, and U. Akgun are with Coe College, Cedar Rapids, IA 52402 USA

L. Ruane is with Hastings College, Hastings, NE 68901 USA

W. Miller is with Shepherd University, Shepherdstown, WV 25443 USA

A. Zieser and D. Wang are with The University of Iowa, Iowa City, IA 52242 USA

U. Akgun is the corresponding author (telephone: 319 399 8597, email: uakgun@coe.edu)

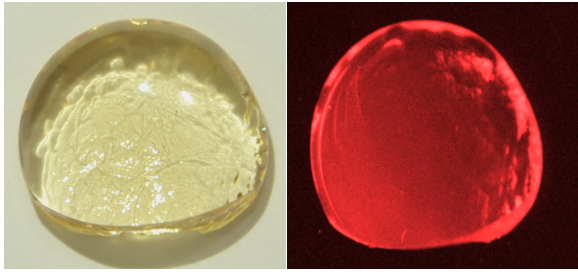


Fig. 1. Pictures of the developed novel glass sample without and with UV excitation. The composition is 0.25 ( $Gd_2O_3$ ) - 0.55 ( $WO_3$ )-0.2 ( $2B_2O_3$ ) (with weight percentages) doped with 1% europium oxide.

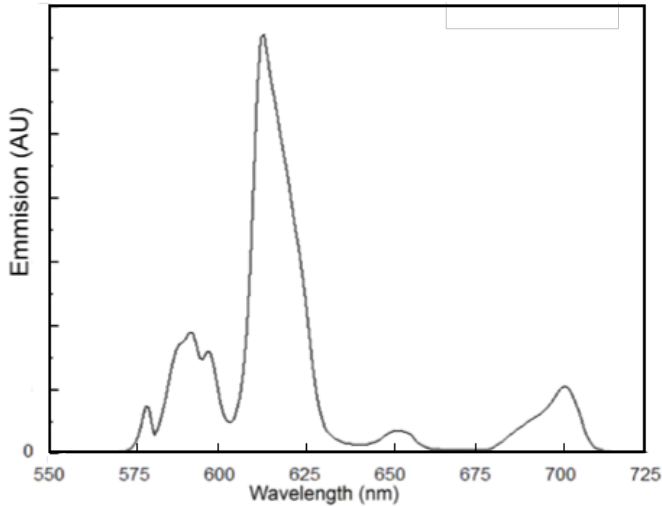


Fig. 2. Emission spectrum of the developed glass sample.

The terbium and europium doped glass samples do not have the danger of transmission cutoff taking over the emission range, at high radiation levels. Both glass samples have transmission cutoffs at around 400 nm, and they have peak emission wavelengths 550 nm (terbium) and 612 nm (europium). In addition to these, the europium doped glass samples had densities of up to  $5.89 \text{ g/cm}^3$ , while terbium and cerium doped samples could barely reach  $5 \text{ g/cm}^3$  densities (see Figure 1). In light of all these considerations, we decided to focus on the novel glass sample: the composition of 0.25 ( $Gd_2O_3$ ) - 0.55 ( $WO_3$ )-0.2 ( $2B_2O_3$ ) (with weight percentages) doped with 1% europium oxide (see Figure 1). The emission spectrum of this selected glass sample is given in Fig. 2.

All glass samples were prepared via the melt-quench technique, with 1200-1500 °C furnace temperatures and platinum crucibles. Transmission spectra were determined with a Perkin-Elmer Lambda 900 UV/Vis/NIR spectrometer, within the range 200-800 nm and using a step size of 1 nm. Excitation and emission spectra were measured with a Jobin Yvon Horiba Fluorolog 3 spectrophotometer. A 450 W xenon arc lamp was used as an excitation source. The emission data was collected at glass's peak excitation and the excitation data was collected at that glass's peak emission wavelength. Density measurements were performed in a Quantachrome micropycnometer using helium gas. The further details of this are given on a previous study [26].

### III. PROOF-OF-CONCEPT DETECTOR DESIGN

The main motivation of this study is to focus on a compact detector design that can be attached to the gantry of a proton therapy system. Unlike in previous approaches, this design eliminates the silicon trackers positioned on both sides of the patient. A single detector performs all tracking and energy measurements. This homogenous calorimeter is capable of stopping 250 MeV protons within 10 cm, due to novel high-density glass developed especially for this application. The compact detector design consists of 70 layers with 100 bars on each layer, with each successive layer oriented at 90 degrees relative to the previous. This unique calorimeter design allows the x-y coordinates, as well as the depth of the Bragg peak, to be determined, both of which are necessary for image reconstruction. Fig. 3 shows simple schematics of the simulated proof-of-concept system. Each bar is made of scintillating glass wrapped in a 95% reflective coating on the sides to trap the scintillation photons. For practical manufacturing purposes, a glass bar size of 1 mm x 1 mm x 100 mm is chosen. A 1 mm x 1 mm glass cross-section is a good match to commercially available SiPM sizes, and a narrower bar size would be very difficult to machine and polish. When photons reach the edges, a SiPM array reads out the signal, which in turn feeds to a data acquisition system, resulting in a measurement of deposited energy within each bar.

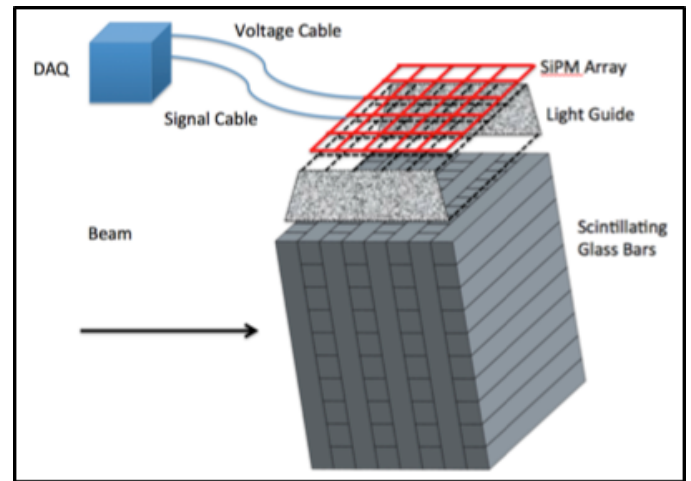


Fig. 3. The schematics of the planned calorimeter, and readout system. The number of glass bars is reduced in the image for visualization purposes.

In order to determine the proton range within the high-density glass, and the energy-depth calibration curve of the protons, the simulation tool [27, 28] was utilized. The performed GEANT4 simulations implemented a number of Physics packages in GEANT4 10.1.p01 including G4EmStandardPhysics, G4QStoppingPhysics, and HadronPhysicsQGSP\_BIC, with special processes G4ProtonInelasticProcess, G4INCLXXInterface and G4BinaryCascade defined for protons.

Protons with energies between 40-140 MeV, with 0.1 MeV increments were shot at the glass calorimeter. The proton generator is positioned 50 cm away from the calorimeter, with no phantom in between. For each energy value,  $10^6$  protons

were used and the depths of individual proton Bragg peaks were determined. Then the Bragg peak distribution for each proton energy was fit to Gaussian. Fig. 4 shows the derived calibration curve showing the proton energy versus the mean depth of the Bragg peak. The error bars are set to standard deviations of the Bragg peak distributions at each proton energy value. Average standard deviation is calculated to be 0.468 mm.

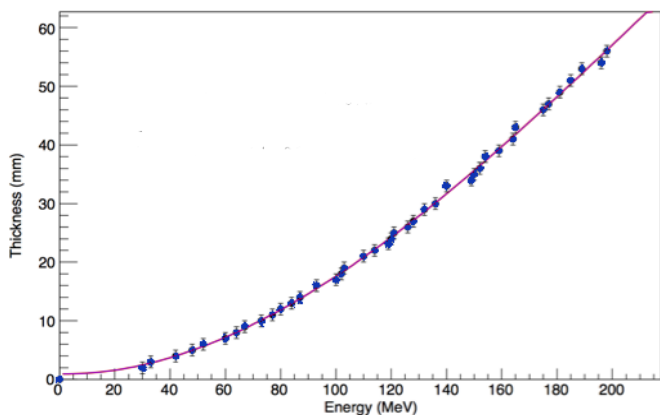


Fig. 4. The proton energy vs Bragg peak location for the selected glass sample.

In addition to eliminating the trackers, this design also aims to use a proton pencil beam instead of shooting individual protons. In our Geant4 simulations  $10^6$  protons in a single spill per second are used to scan the Shepp-Logan phantom. Because the individual proton scattering is isotropic, the center of the beam spill can be tracked for image reconstruction, and the highest energy deposition and light yield occur at the center of the pencil beam. If applied successfully, this approach will allow us to reduce the data acquisition time.

The alternating orientations of the scintillating glass bars allow the elimination of tracker systems utilized in previous studies<sup>12,17</sup>. With the current design, the first two layers give initial x-y coordinate within the calorimeter, and the second two layers give a second set of x-y coordinates - two or more sets of coordinates are sufficient to know the direction of the proton beam. Energy deposition within the calorimeter is monitored via light production at each layer. The highest scintillation yield in a layer will be the average Bragg peak location that gives the average individual proton energy, hence the total energy deposited within the phantom. Our simulations show that the 10 cm depth in the calorimeter is good enough to contain all of the beam particles with no leakage. The initial beam energy and momentum, along with the measured momentum and energy of the beam after the phantom are the final variables that can be used for image reconstruction.

#### IV. IMAGE RECONSTRUCTION STUDIES

For proof-of-concept 2D imaging studies, the pCT scan data were generated via Geant4 simulation. A standard 3D Shepp-Logan phantom model was used for these 2D scan studies. In the Shepp Logan model, the densities are set to these values: outer cortical bone  $1.85 \text{ g/cm}^3$ , adipose tissue  $0.92 \text{ g/cm}^3$ ,

striated muscle  $1.06 \text{ g/cm}^3$ , water  $1 \text{ g/cm}^3$ . More detailed description and the image of the simulated model can be found in a previous publication [29].

During the simulated scan, the Shepp-Logan phantom was positioned 20 cm from the proton generator, and the calorimeter was 30 cm behind the phantom.  $10^6$  protons, with 200 MeV energy, were shot from the same initial coordinate and allowed to scatter in the air. The simulated proton pencil beam spread reaches to 3 mm when it arrives to the phantom, and after the phantom the spread increases to 17.3 mm; however the mean x and y position of the whole beam stays practically unchanged. The x-y coordinate deviations of the proton-spill-center are less than 0.004 mm at the phantom and less than 0.06 mm at the calorimeter. The CT scan step size of 1 mm was chosen for this proof-of-concept study. After finishing one line of scan, the phantom was rotated by  $2^\circ$ , and these steps were repeated 180 times to complete a full circle (see Fig. 5). The preliminary image optimization was performed over variables such as the initial proton distance from the phantom, detector bar size, step size of the scan, and the initial beam energy [29].

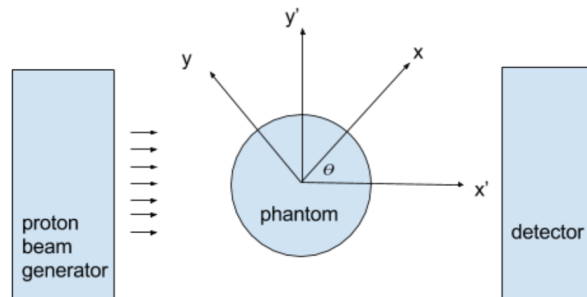


Fig. 5. The schematics of the simulated 2D pCT scan. The proton beam with  $10^6$  particles scans the phantom with 1 mm step size. Then the phantom is rotated by 2 degrees, and the scan is repeated until 360 degree rotation is completed.

The calorimeter design provides exit data from the phantom for each proton spill, including energy, along with coordinates and momenta, both of which can be calculated from the energy. The data can be used to estimate the path taken by each beam through the patient. This is the first necessary step in full image reconstruction. There are a number of methods for approximating the proton path within the phantom. In the proof-of-concept study we utilized two of them:

- i) Straight Line Path (SLP) approximation considers the path of each proton beam as a straight line, and therefore it needs only to take into account the starting and ending locations – their momenta are irrelevant for this method. As evidenced by the current status of the work by our group, deviations from a straight line are small enough that this path estimation can give encouraging results.
- ii) Cubic Spline Path (CSP) approximation uses both the location and direction to generate a path in the shape of a cubic polynomial within the phantom. This is a trivial mathematical process equivalent to estimating any cubic polynomial using two known points and two known derivatives.

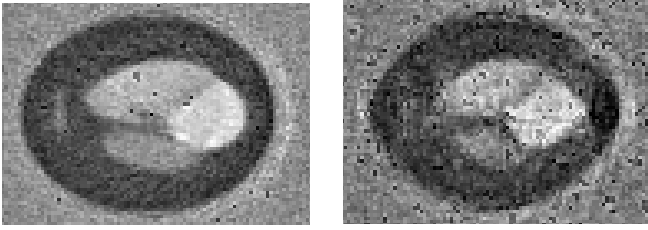


Fig. 6. The reconstructed images from 190 MeV pCT scan of the Shepp-Logan phantom, with SLP (LEFT), and CSP (RIGHT) approximations.

In each case the image reconstruction code used modified simultaneous algebraic reconstruction technique (SART), to map the proton stopping powers. Then the ratio of mass stopping powers was determined by dividing proton stopping powers by the object's density. Bethe's stopping formula is used to describe the specific energy loss for a particle within the material (more detailed description of the reconstruction method can be found in [30]).

Fig. 6 shows the reconstructed images from the Geant4 simulated 190 MeV pCT scan of the Shepp-Logan phantom, utilizing SLP and CSP approximations.

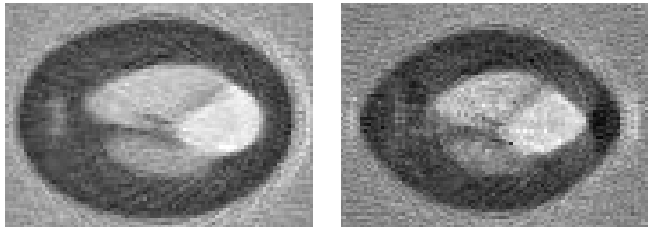


Fig. 7. The reconstructed images from 190 MeV pCT scan of the Shepp-Logan phantom, with SLP (LEFT), and CSP (RIGHT) approximations. Splitting the total energy deposited into the calorimeter to the top 9 signal yielding glass bar coordinates creates these images.

It should be noted that these imaging efforts are only proof-of-concept, and there are huge room for improvement. For example, since a pencil beam is used during the simulated CT scan in the first try we assigned all the deposited energy of the beam to the location of the Bragg peak. This may sound like a reasonable approach since the center of the spill goes almost straight. However, as a first order correction, we developed an offline addition to the imaging code that splits the energy distribution to the top 3, 5, 7, 9, 11, 13, 15 energy deposited glass bars. When this splitting was applied, the reconstructed images started to appear smoother. Fig. 7 shows the same images reported on Fig. 6, with the total energy deposition in the calorimeter split into the to 9 top signal yielding glass bar locations.

## V. CONCLUSION AND DISCUSSION

This study aims to show the feasibility of a compact, proton imaging detector that can be attached to the gantry. The physical and optical properties of the developed novel high-density glass are reported. The current glass candidate is 5.9 g/cm<sup>3</sup> Europium doped Gd<sub>2</sub>O<sub>3</sub>-WO<sub>3</sub>-B<sub>2</sub>O<sub>3</sub> system. If the scintillator signal becomes an issue due to DAQ speed or the timing between the spills of protons, we propose to use Cerium as the scintillating dopant. High-density glass sample

with Cerium (signal speed is ~10ns) has been successfully produced, however the light yield and density is not at the level of the sample used in this study.

The Geant4 studies show that the glass bar thickness is the limiting factor on the detector resolution. However, the design requires SiPM readout system, and 1 mm x 1 mm is a standard size for commercial SiPMs. In the proof-of-concept study only SLP and CSP approximations were utilized. In future studies, we plan to test other approaches, such as the most probable path (MPP), and back projection technique to improve the resolution of the final image.

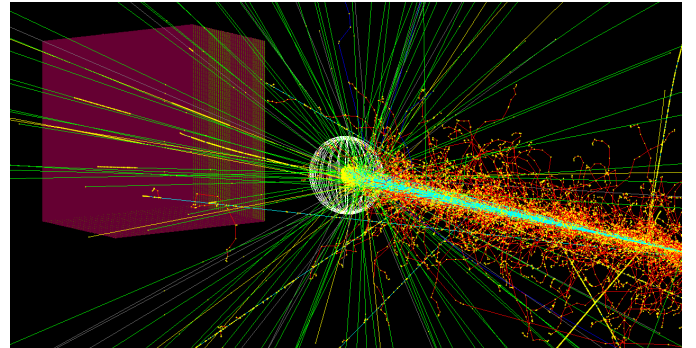


Fig. 8. Screenshot from Geant4 simulations of the hadron therapy revealing the prompt gammas (green lines) interacting with CARNA.

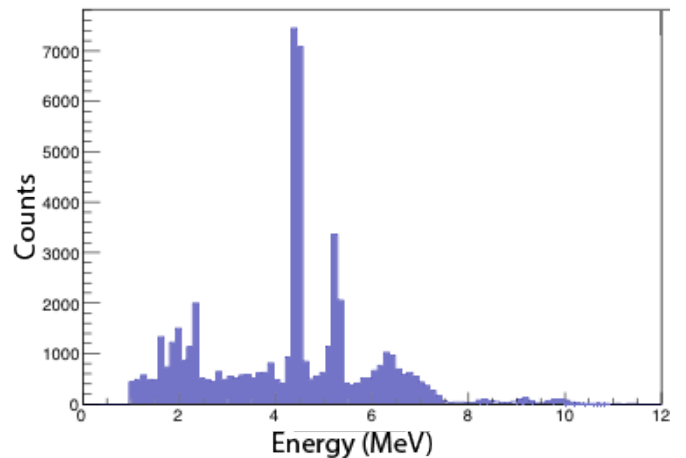


Fig. 9. Energy distribution of the prompt gammas generated at the Bragg peak in Geant4 simulations.

The ability to use the proton beam therapy is limited due to the error in predicting the location of the Bragg peak and determination of the beam range. Even with the improved imaging by using the pCT, the exact reproduction of the planned patient alignment is not possible. However, *in vivo* imaging can be used to minimize the overshooting or undershooting of the tumor, which otherwise result in damaging the healthy tissue. Protons make three distinct secondary emissions within the human body: thermoacoustic, positron annihilation gammas, and prompt gammas<sup>32,33</sup>. The described detector can easily detect the prompt gammas, ranging 2-15 MeV energies. Considering the fact that regular PET devices are not effective in this high-energy range, CARNA can be implemented into hadron therapy devices to perform *in vivo* imaging, as well. Fig. 8 and Fig. 9 show a screenshot of the Geant4 simulations we performed to

simulate the prompt gamma events in our system, and the energy distribution of the prompt gammas generated during the hadron therapy within the human body. With the added prompt gamma detection capabilities for *in vivo* range detection, this proton imager has potential to drastically improve hadron therapy accuracy<sup>12-13</sup>.

Future directions of the work include the construction of a physical proof-of-principle detector prototype with high-density scintillating glass bars. There is also a lot of room for improvement by using different imaging geometry and reconstruction algorithms. A future prototype needs to be tested with actual proton pencil beams.

#### ACKNOWLEDGMENT

This work was funded by NSF-DMR 1407404, NSF-REU 1358968, The University of Iowa FUTURE in Biomedicine Program, R.J. McElroy Trust Student/Faculty Research Fund. The authors are thankful to Dr. Luiz Jacobsohn and Clemson University COMSET, and Prof. Madeline Shea of University of Iowa for the amazing support they provided for this project.

#### REFERENCES

[1] Denyak V. V. *et al.*, "Dose energy dependence in proton imaging", Nuclear Instruments and Methods A, 652, 747-750, (2011).

[2] Mumot M. *et al.*, "Proton range verification using a range probe: definition of concept and initial analysis," Physics in medicine and biology 55, 4771 (2010).

[3] Telsemeyer J. *et al.*, "Quantitative carbon ion beam radiography and tomography with a flat-panel detector," Physics in medicine and biology 57, 7957 (2012).

[4] Bopp C. *et al.*, "Proton computed tomography from multiple physics processes," Physics in medicine and biology 58, 7261 (2013).

[5] Martisikova M. *et al.*, "Test of an amorphous silicon detector in medical proton beams", Nuclear Instruments and Methods A, 633, S259-S261, (2011).

[6] Civinini C. *et al.*, "Towards a proton imaging system", Nuclear Instruments and Methods A, 623, 588-590, (2010).

[7] Sipala V. *et al.*, "A proton imaging device: Design and status of realization", Nuclear Instruments and Methods A, 612, 566-570, (2010).

[8] Knopf A. C., *et al.*, "Accuracy of proton beam range verification using post-treatment positron emission tomography/computed tomography as function of treatment site," International Journal of Radiation Oncology Biology Physics 79, 297-304 (2011).

[9] Cormack A. M., "Representation of a function by its line integrals, with some radiological applications." J. Appl. Phys. 22, 2722-2727 (1963) [doi:10.1063/1.1729798].

[10] Cormack A. M., "Representation of a function by its line integrals, with some radiological applications. II," J. Appl. Phys. 35(10), 2908-2913 (1964) [doi:10.1063/1.1713127].

[11] Koehler A. M., "Proton Radiography" Science. 160, 303 (1968)

[12] Cormack A. M. and Koehler A. M., "Quantitative proton tomography: preliminary experiments," Phys. Med. Biol. 21(4), 560 (1976) [doi:10.1088/0031-9155/21/4/007].

[13] Hanson K., "Proton Computed Tomography," Comput. Aided Tomogr. Ultrason. Med.(1), 97-106 (1979) [doi:10.1142/S0217732315400246].

[14] Hanson K. M. *et al.*, "Computed tomography using proton energy loss," Phys. Med. Biol. 26(6), 965 (1981) [doi:10.1088/0031-9155/26/6/001].

[15] Hanson K. M. *et al.*, "Proton computed tomography of human specimens," Phys. Med. Biol. 27(1), 25-36 (1982) [doi:10.1097/00004728-198208000-00062].

[16] Bushberg J. T. *et al.*, [The Essential Physics of Medical Imaging, 3rd Ed.] Lippincott Williams & Wilkins, PA (2012)

[17] Parker R. P., Hobday P. A, and Cassell K. J., "The direct use of CT numbers in radiotherapy dosage calculations for inhomogeneous media," Phys. Med. Biol. 24(4), 802-809 (1979) [doi:10.1097/00004728-198002000-00045].

[18] Mustafa A. A. and Jackson D. F., "The relation between x-ray CT numbers and charged particle stopping powers and its significance for

radiotherapy treatment planning," Phys. Med. Biol. 28(2), 169-176 (1983) [doi:10.1088/0031-9155/28/2/006].

[19] Schneider U., Pedroni E., and Lomax A., "The calibration of CT Hounsfield units for radiotherapy treatment planning," Phys. Med. Biol. 41(1), 111-124 (1996) [doi:10.1088/0031-9155/41/1/009].

[20] Schneider U., "Proton radiography as a tool for quality control in proton therapy," Med. Phys. 22(4), 353 (1995) [doi:10.1118/1.597470].

[21] Schneider U. *et al.*, "First proton radiography of an animal patient," Med. Phys. 31(5), 1046-1051 (2004) [doi:10.1118/1.1690713].

[22] Schneider U. and Pedroni E., "Multiple Coulomb scattering and spatial resolution in proton radiography," Med. Phys. 21(11), 1657-1663 (1994) [doi:10.1118/1.597212].

[23] Zygmanski P. *et al.*, "The measurement of proton stopping power using proton-cone-beam computed tomography," Phys. Med. Biol. 45(2), 511-528 (2000) [doi:10.1088/0031-9155/45/2/317].

[24] Schulte R. *et al.*, "Conceptual design of a proton computed tomography system for applications in proton radiation therapy," IEEE Trans. Nucl. Sci. 51(3 III), 866-872 (2004) [doi:10.1109/TNS.2004.829392].

[25] Plautz T. *et al.*, "200 MeV proton radiography studies with a hand phantom using a prototype proton CT scanner," IEEE Trans. Med. Imaging 33(4), 875-881 (2014) [doi:10.1109/TMI.2013.2297278].

[26] Tillman I. J. *et al.*, "High-Density Scintillating Glasses For A Proton Imaging Detector" Journal of Optical Materials, 68, 58-62, 2017

[27] Agostinelli S. *et al.* "Geant4 - A Simulation Toolkit", Nucl. Instr. and Meth. A, 506 (2003) 250-303

[28] Allison J. *et al.*, "Geant4 Developments and Applications", IEEE Trans. on Nucl. Sci., 53, No. 1 (2006) 270-278

[29] Wilkinson C. J. *et al.*, "High density scintillating glass proton imaging detector", Proc. SPIE 10132, Medical Imaging 2017: Physics of Medical Imaging, 101323V; doi:10.1117/12.2252777; 2017

[30] Wang D., Ph.D. Dissertation, University of Wisconsin-Madison (2011)